

We are IntechOpen, the world's leading publisher of Open Access books Built by scientists, for scientists

6,900

Open access books available

186,000

International authors and editors

200M

Downloads

Our authors are among the

154

Countries delivered to

TOP 1%

most cited scientists

12.2%

Contributors from top 500 universities



WEB OF SCIENCE™

Selection of our books indexed in the Book Citation Index
in Web of Science™ Core Collection (BKCI)

Interested in publishing with us?
Contact book.department@intechopen.com

Numbers displayed above are based on latest data collected.
For more information visit www.intechopen.com



Multimodal Imaging of Hepatocellular Carcinoma Using Dynamic Liver Phantom

*Muntaser S. Ahmad, Osama Makhamrah
and Mohammad Hjouj*

Abstract

Liver phantom is used at various medical levels, such as detecting hepatocellular carcinoma (HCC) in the early stages, training medical staff to deal with HCC by taking biopsies, developing new sequences on medical imaging devices, confirming the image quality, applying treatments to HCC, and others. All of the trials should be applied before entering the real human body. The phantom includes properties very similar to those of the human body, as well as the properties of liver cancer and how it is treated within the body through its biological form. Therefore, the present chapter aims to provide comprehensive information to consider when fabricating HCC-containing phantoms and the characteristics of those phantoms in proportion to multimodal medical imaging to aid in understanding the main target of dynamic phantom for HCC.

Keywords: Liver phantom, HCC, Dynamic Phantom, Multimodality Imaging, phantom characteristic

1. Introduction

Cancer is one of the most common diseases in the world and threatens human life on an unprecedented scale. Hepatocellular carcinoma (HCC) is one of the cancer types that originate in the human liver, and usually, it discovers at a late stage [1, 2]. The detection of HCC at the early stage increases the clinical efficacy of treatment by 60% compared to late detection. Several methods are used to detect HCC; alpha-fetoprotein (AFP); Ultrasound (US); computed tomography (CT); magnetic resonance imaging (MRI); and hybrid fluorodeoxyglucose positron emission tomography with FDG PET/CT [3].

The difficulties of detecting liver cancer in its early stages lie with researchers and medical practitioners. Therefore, researchers need to provide any method that will enable them to achieve this goal. Thus, the researchers turned to a tool that can be used to detect liver cancer before the actual application to the real patient. One such tool is the phantom, which mimics hepatocellular carcinoma [4, 5].

2. Diagnosis of HCC

HCC is detected in several medical methods, one of which is the use of non-invasive medical imaging technology. For HCC, the detection depends primarily on the detection of vascular perturbation of cancer. Therefore, contrast media enhancement is used in medical imaging techniques, which are relied upon to detect these disorders through the three imaging phases: late arterial phase, Porto-venous phase (PVP), and delayed phase.

The HCC is supplied by the hepatic artery, while the normal liver parenchymal cells are nourished by the portal vein. Based on this information, it is possible to distinguish between HCC and normal liver cells by contrast enhancement in both CT and MRI scans. The HCC cells show hyper-vascularity in the late arterial phase, while in the Porto-venous phase it appears less bright because it contains blood free of contrast (washout), and these features are known as classic features. These characteristics of cancer depend on the size of cancer itself, as the early stages of cancer do not have a large blood supply, in this stage are usually less than 1 cm in size, but in the advanced stages of cancer, it reaches 1-2 cm or more [6, 7].

2.1 HCC diagnosis in CT and MRI

The sensitivity of both CT and MRI to detect HCC varies according to HCC size. The sensitivity of MRI reaches 62% compared to 48% in CT for the HCC of less than 2 cm, while it reaches 95% in MRI compared with 92% in CT for HCC more than 2 cm. The major difference in both modalities lies in the detection of lesions less than 1 cm. Although MRI shows better results than CT, both have low specificity [8].

The image characteristics of both MRI and CT scans are similar in detecting liver cancer through the use of contrast enhancement. It appears as a very bright (strong signal) in the arterial phase and is less bright (lower signal) in the porto-venous phase and in the delay phase, it appears black. However, in MRI it appears hyper-intensity also on T2-weighted and diffusion-weighted images. A specific contrast agent is used in the MRI to increase the sensitivity of the examination in the detection of HCC, which is the gadolinium-ethoxybenzyl-diethylenetriamine pentaacetic acid (Gd-EOB-DTPA, Primovist, or Eovist). The reason is that only 50% of gadoxetic acid is absorbed into the liver cells and it is excreted by bile ducts and the remaining 50% is excreted by the kidneys [9].

In the arterial stage, the excessive enhancement this stage is caused by increases in the arterial supply of the nodules. While the washout appearance in the PVP and delayed phase depends on different factors such as the new drainage in the veins, the liver background enhancement, the amount of blood supply in the portal vein, the hyper-cellularity rate of a tumor, and the fundamental components of the cancer tissue. Indeed, the hemodynamic changing in the nodules through the development of carcinogenesis starts with decreasing the arterial supplies and presence of portal perfusion, after that the decreases on both arterial supplies and portal blood supplies would occur. Subsequently, the increase of arterial vascularity is developed, and the hypervascular pattern would appear [10]. **Figure 1** shows the typical features for HCC in MRI and **Figure 2** Shows a typical pattern of HCC in CT.

2.2 Contrast-enhanced ultrasound

Contrast-enhanced ultrasound (CEUS) can be used in ultrasound imaging to detect HCC. However, the possibility of error in diagnosis is high in this technique,

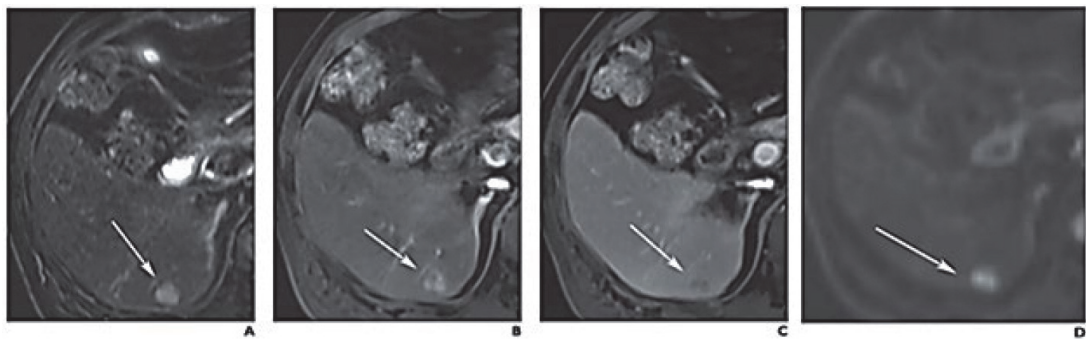


Figure 1.
Typical enhancement patterns of HCC; (A): Hyperintensity on T2 weighted image; (B): Arterial enhancement (arrow) on arterial phase image; (C): Tumor shows washout on portal venous phase image; and (D): Diffusion restriction on DWI [11].

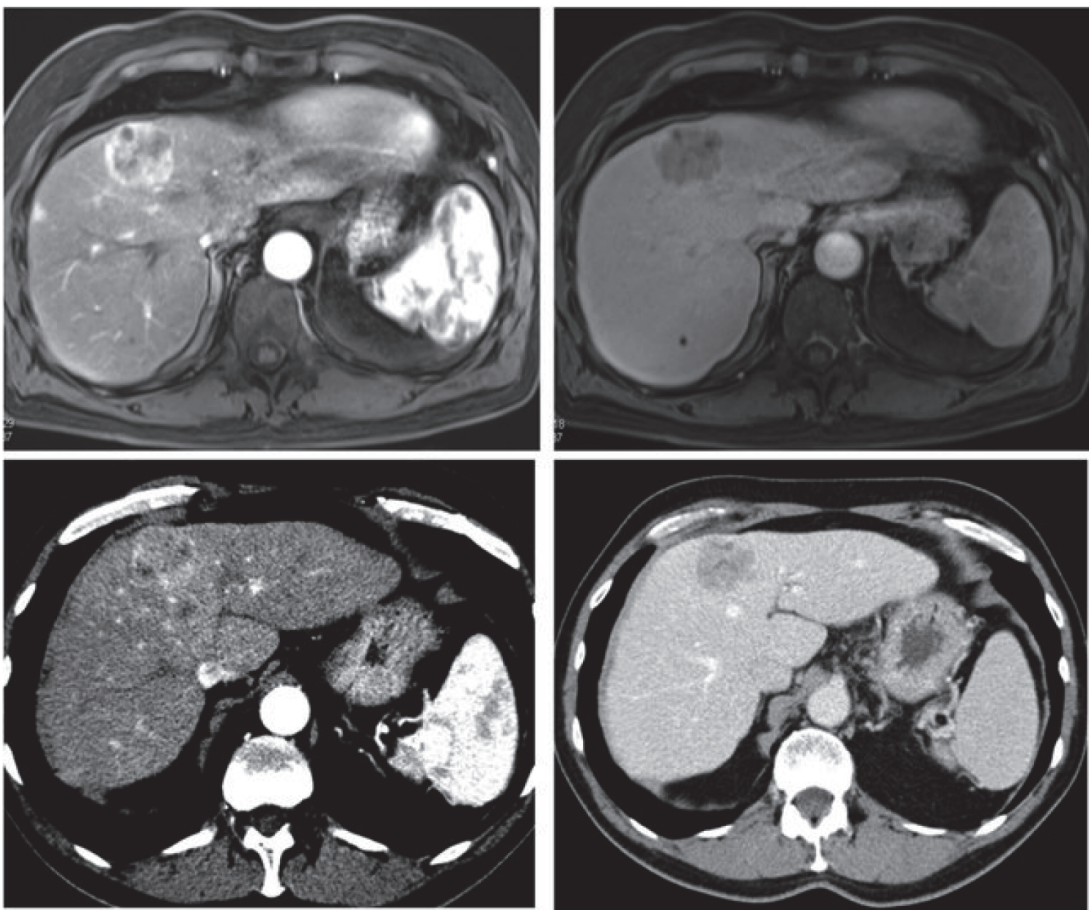


Figure 2.
Typical vascular pattern of HCC in CT: Liver lesion in the right hepatic lobe observed in a cirrhotic patient. The lesion is presenting a typical HCC vascular pattern with arterial hyperenhancement (left images) and venous wash-out (right images) visible both in magnetic resonance imaging (MRI) (upper row) and computed tomography (CT) (lower row) [12].

due to the rapid washout of the CEUS in less than 60 seconds after contrast material injection, and thus increases the risk of diagnostic error [7].

The contrast media used in CEUS such as sulfur hexafluoride and octafluoropropane combined with a phospholipid shell has a short arterial phase, so the liver exploration is not adequate to visualize the deep lesions [13]. Another problem with ultrasound is the inability to review the output image. CEUS and contrast enhanced MRI in lesions less than 2 cm can be used to improve diagnosis [14].

2.3 FDG-PET/CT

FDG PET/CT imaging is based on molecular imaging in different diagnoses of cancers. HCC is characterized by a low uptake of the FDG, and therefore the sensitivity of the examination is reduced compared with MRI and CT. Where it reaches less than 70%. In addition, normal liver cells absorb FDG significantly, and thus the sensitivity of detecting HCC than normal cells would be less [15].

3. Liver dynamic phantom component for hepatocellular carcinoma

3.1 Liver phantom

Different liver MRI phantoms are commercially available, that mimics blood vessels structures, tumor models, and real appearance [16]. However, none of them is a dynamic phantom. There are many commercial phantoms that offer 3D liver designs, but they are quite pricey. Therefore, we need to fabricate a liver phantom that is available at a lower cost. These phantoms use in multimodal medical imaging (US, CT and MR) such as CIRS model 057A [17], IOUSFAN® phantom [18], and Quality Assurance in Radiology and Medicine (QRM) GmbH supplies another version of a semi-anthropomorphic liver phantom (QRM-Abdomen Phantom, QRM GmbH, Möhrendorf, Germany) [19].

In previous studies, many chemical materials have been used to fabricate the human liver as TMMs. Most of these materials are represented on carrageenan [20], Poly Acrylic Acid (PAA), agar, PolyVinyl Alcohol (PVA) [21], polysaccharide, agarose [22], gelatin and silicone [23], polyurethane [4], commercial rigid plastics [24], and elastomeric (rubber-like) materials [25]. Shevchenko et al., (2011) [26], and Chmarra et al. (2013) [27], developed a phantom to simulate the liver using candle gel with cellulose. The simulation included the liver blood vessels in a simple form and the phantom was used for CT and US imaging. Another study conducted by Rethy et al. (2018) [4], using polyurethane to simulate the liver due to its durability. The phantom involved the simulation of the arterial and venous system of the liver with high accuracy as it was the first phantom that applying the contrast media. Phantom has been used on various medical modalities including CT, MRI, and US. All of Advantages and disadvantages of chemical materials for phantom fabrication were summarized in Appendix A.

The liver phantoms were increasingly used in clinical practices for different purposes including medical training and education, surgical and interventional planning, diagnosis and treatment planning, and research aims. Qiu et al., (2018) [25], developed a 3D phantom used as a surgical assistant for various human organs to provide an effective pre-operative planning solution. The study used rigid-plastic materials to create and develop a body that mimics the human liver. Another study conducted by Zein et al. (2013) [28], in the development of a human liver model using the PolyJet process, where simulated three liver models of three liver donors. These phantoms were used in anatomical evaluations before and during the surgical procedure. Javan and Zeman, (2018) [24] developed a 3D-printed model using polyamide material to fabricate the liver. The study was conducted for liver anatomical evaluation and to develop advanced functional interventional liver phantom. With a different purpose of the phantom, Bazrafshan et al. (2014) [29], developed a liver phantom made of acrylamide gel used in the development of tools for thermal mapping and coagulation progress which is applied in thermal tumor ablation methods such as radiofrequency ablation, and laser-induced interstitial thermotherapy.

3.2 HCC phantom

Several previous studies have included liver phantom within HCC samples. All of these studies focused on differentiating between normal liver cells and HCC by varying the density, intensity, and echogenicity for CT, MRI, and US, respectively. However, none has dealt with HCC samples in a dynamic way that simulates three phases; Arterial phase; Porto-venous phase; and Delayed phase, as in typical HCC.

Rethy et al. (2018) [4], designed a phantom similar to the human liver. This design contained HCC made of polyurethane blended with calcium carbonate. Where they used the concentration of –100 parts by weight (pbw) of polyurethane and 0.6% of Sephadex added with 5% calcium carbonate bw. Chmarra et al. (2013) [27], also designed another human liver phantom, including HCC samples which is made from agarose, with glycerol. The samples were made with 7.5 g of agarose, 30 ml of glycerol, 200 ml of distilled water, and 4 g of sephadex. The phantom was applied to various medical modalities and showed similar results to human tissue characteristics. In addition, the Javan and Zeman, (2018) [24] developed a 3D phantom of the liver containing cancer samples using polyamide material. The normal liver cells were distinguished using resin while polymer was used to simulate the internal structures which is allowed the catheters and wires for passing. In contrast, Shevchenko et al. (2011) [26], developed a liver phantom including tumor model made from agarose-glycerol mix. The phantom was applied under CT and US imaging while it was not applied under MRI. K. Li et al., (2017) [30] conducted a study of Evaluation of the ablation margin of hepatocellular carcinoma for testing Radiofrequency ablation on the HCC which was made from carrageenan. The phantom was applied in CEUS, CT, and MRI.

3.3 Dynamic phantom

Dynamic contrast-enhanced (DCE) imaging is a method used to measure the kinetic perfusion of tumors within the body. It is also used to simulate the motion of blood circulatory inside the organ and to improve the diagnostic value, radiation treatment planning, treatment effectiveness, and monitoring [31]. This technique was used to simulate the perfusion in different tissues. However, most of the capillaries could not be imitated accurately [32]. This technique relies on the dynamic movement of contrast agent (CA) through different tissues. Therefore, the technique depends on the measurement of time-attenuation curves (TAC) for CA through the intra-arterial, intra-venous, and delay phases. The differences of CA physio-chemical properties such as solubility, viscosity, and electric charge effect on tumor pharmacokinetics [32].

The quantitative parameters such as blood flow, permeability, and blood volume control the amount of blood supply to the cancer cell. Each stage of cancer requires a different blood perfusion. Thus, it is possible to simulate the stages of cancer through DCE technique. There are several issues that need to be considered when using dynamic phantom. The phantom should be in a container that allows the transfer of contrast material from the arteries to the veins through the study samples, the substance of the sample should possess the appearance of HCC, the sample should interact with the contrast material, the sample should work to remove the contrast material without altering the sample structure, flexibility regarding changing the HCC samples without affecting the liver parenchyma structure, and the phantom should allow the pumping and disposal process of the contrast material by using an automatic injector and suction device [33, 34].

4. Phantoms properties-related modality

In order to use the phantom instead of the human tissue, different human tissue characteristics must be present in the phantom. In addition, when simulating an organ of human body, the shape, size and characteristics of the phantom must be similar to that organ. The materials used in the simulation must be non-toxic, non-degradable over time without change in properties, easy to manufacture and inexpensive. Each medical imaging modality has its own features to detect a special tissue characteristic, the features must exist in the manufactured Phantom to mimik the human biological tissue. An explanation of these characteristics to be available in the Phantom according to medical imaging modality type.

4.1 Computed tomography

The phantom fabricated to CT device should has the same mass density (ρ_m) resulting in the same CT numbers or Hounsfield units (HU), same linear attenuation coefficient (AC), same effective atomic number (Z_{eff}), and the same electron density (ρ_e) of the human tissue [16]. CT numbers can be calculated by the Eq. (1) [35]:

$$CTnumber(HU) = \frac{\mu_{tissue} - \mu_{water}}{\mu_{water}} * 1000 \quad (1)$$

While the linear attenuation coefficient (μ) can be calculated using the Eq. (2):

$$I_x = I_0 * e^{-\mu x} \quad (2)$$

While the effective atomic number (Z_{eff}) can be calculated through the Eq. (3):

$$Z_{eff} = \sqrt[n]{w_1 Z_1^x + w_2 Z_2^x + w_3 Z_3^x + \dots + w_n Z_n^x} \quad (3)$$

Finally, the electron density (ρ_e) and mass density (ρ_m) are calculated using the Eq. (4):

$$\rho_e = \rho_m * NA * Z/A \quad (4)$$

Where μ_{tissue} is the linear attenuation coefficient for the tissue, μ_{water} is the linear attenuation coefficient of water, I_x is x-ray intensity after interact with human tissue, I_0 is x-ray intensity before interact with human tissue, x is the human tissue thickness, w_n is the number of atom Z_n in the compound, Z_n is the atomic number of the element, NA is the Avogadro's number, and A is the atomic mass of the element [16].

4.2 Magnetic resonance phantoms

The majority of MRI phantoms are represented in a fluid-filled model. These phantoms differ in their dimensions and forms depending on the body organ to be simulated. The phantoms are fabricated in order to achieve several purposes including evaluate image contrast, evaluate image uniformity, estimate spatial resolution, improve the signal-noise ratio (SNR), check the accuracy of slice thickness, and achieve geometric accuracy.

MRI phantom should have several characteristics compatible with MRI technology, these characteristics include tissue-specific relaxation for both; longitudinal relaxation time (T1) and transverse relaxation time (T2); variation of signal intensity with temperature changing; the mechanical properties should be fixed over an

extended period [36]; and the phantom should be suitable to fit in the existing MRI coils [37]. The recovery time and decaying time depend on molecular motion in the local environment. Thus, T1 and T2 relaxation times changing with different diseases such as inflammation, hemorrhage, and any biological dysfunction. Also, the T1 and T2 relaxation times depend on tissue rigidity and viscosity. Low signal intensity on T1W and T2W appears when using phantom materials with greater viscosity and higher rigidity.

MRI phantoms have been manufactured using either aqueous solutions or polymer gels. Aqueous solutions are usually doped with paramagnetic ions like MnCl₂, CuSO₄, GdCl₃, and NiCl₂. These materials are used for testing MRI equipment because it has the property of stability. However, they are affected by motion artifacts and need a container to maintain shape [36]. Regarding gel phantoms, a lot of materials have been used in the literatures for fabricating MRI phantom including gelatin [38], gelatin-agar [39], agarose [40], agar [41], PVA [42], polysaccharide TX-150 [43], polysaccharide TX-151 [44], PAA [45], room-temperature-vulcanizing (RTV) silicone [46], and carrageenan [30, 47].

The properties of materials used to fabricate the MRI phantom are categorized into four groups including chemical properties, mechanical properties (density, pressure, elasticity, and hardness), electrical properties (conductivity and permittivity), and imaging properties (relaxation times T1 and T2). The chemical properties of the material examine using several vibrational spectroscopic techniques (VST). Different VST was used to know the chemical properties of the different samples including Fourier transform infrared spectroscopy (FTIR) [48], Near-infrared spectroscopy (NIRS), Mid-infrared Spectroscopy (MIR), Raman spectroscopy, and hyperspectral imaging (HSI) [49].

The mechanical properties of the phantom are among the most important properties that should be taken into considerations to give the best simulation of the human body organs. These properties consist of density, compressive modulus, elastic modulus, and toughness. Density depends on the quantity of mass per unit volume. The material densities should be around $1.03 \pm 0.04 \text{ g/cm}^3$ which is closed to human tissue density [50]. The concentration of materials used in the phantom fabrication manipulates until reaches the suitable human tissue density. To confirm the stability of phantom density, several readings take overtime to monitor any density changes for phantom materials. Compressive modulus or compressibility expresses the material's ability to withstand pressure without changing the shape or size. The unit of compression strength is the pascal (Pa). Different models are used to measure the compression modulus such as the standard test method used for polymers; flexible cellular polymeric materials used for cellular [51]; and tensile strength for fused filament fabrication [52]. According to these models, the compressive strength measurements are different. Instron compression-testing machine is widely used in estimating compressive strength.

An electric is any insulated object that polarizes through applying an electric field. The most common property used in electricity is conductivity (σ) which is varied with frequency. For example, liver conductivity increases with increasing frequency [53]. Conductivity is the amount of resistance of the material or a material's ability to conduct electrical current. The signal intensity unit of electrical conductivity is siemens per meter (S/m or S.m⁻¹) [54]. The dielectric Win DETA 5.64 from Novocontrol Technologies is used to measure the polymer dielectric properties.

4.3 Ultrasound

The phantom fabricated in the ultrasound should have the same velocity of sound or acoustic velocity, same Attenuation coefficient (AC), same acoustic

impedance (Z), and same backscatter coefficient of the human tissue [55, 56]. The acoustic velocity (C_s) can be calculated by the Eq. (5):

$$C_s = \left(\frac{d_p}{d_\rho} \right)^{0.5} = \left(\frac{k_s}{\rho} \right)^{0.5} \quad (5)$$

While the Attenuation coefficient (α_s) in the ultrasound can be calculated through the Eq. (6):

$$\alpha_s = \alpha_w - \frac{1}{\Delta x} (\ln A_s - \ln A_w - 2 \ln [1 - R]) \quad (6)$$

The R magnitude can be calculated by this Eq. (7):

$$R = \frac{Z_2 - Z_1}{Z_2 + Z_1} \quad (7)$$

The Backscatter coefficient (BS) is calculated by the Eq. (8):

$$BS(f, z) = \frac{S_s(f, z)}{S_R(f, z)} BS_R(f, z) A(f, z) \quad (8)$$

Where d_p is the pressure change in Pascal, d_ρ is the change of density in Kg.m-3, k_s is the modulus of bulk elasticity, α_w is the water attenuation coefficient, A_s is the ultrasound pulse amplitude, A_w is the water amplitude, R is the coefficient of acoustical reflection at the interface between material and water itself, Z_2 is the acoustic impedance of the material, Z_1 is the acoustic impedance of the water, S_s is the sample spectra, S_R is the phantom spectra, BS_R is the reference phantom backscatter, A is compensates function for attenuation along the propagation path, f is the frequency of ultrasonic wave, and z is the region depth of analysis [16].

4.4 Scintillation camera imaging

The following characteristics should be present on the phantom under scintillation camera imaging: same sensitivity, spatial resolution, count rate linearity, and contrast recovery of some radiopharmaceuticals such as ^{99m}Tc , ^{90}Y , and ^{166}Ho [57]. The Calibration factor (CF) can be calculated by the Eq. (9):

$$CF_{cps/Bq} = cps/A \quad (9)$$

While the sensitivity (S) or minimum detectable activity can be calculated through the Eq. (10):

$$S = \frac{4.65 \sqrt{N}}{CF * t} + \frac{3}{CF * t} \quad (10)$$

Where cps is count per second of the phantom, A is the activity amount inside the phantom, N is the total background counts of the region of interest and t is the count time [16].

5. Conclusions

In summary, in order to achieve the best simulation of hepatocellular carcinoma, researchers should investigate as much as possible the characteristics of this disease

and how it behaves inside the real human body. It varies from stage to stage, and therefore the simulation of HCC should be in a specific for each stage and likes to take into account the size of the cancer and the blood supply to it in each stage. Then the characteristics of the phantom should match with the characteristics of the multimodality imaging to be used for screening.

Acknowledgements

We would like to acknowledge the Universiti Sains Malaysia staff especially Dr. Nursakinah Suardi, Proff. Ahmad Shukri, and Dr. Nik Noor Ashikin Nik Ab Razak for supporting our research.

Conflict of interest

The authors declare no conflict of interest.

Appendices and nomenclature

Advantages and disadvantages of chemical materials for phantom fabrication.

| Material | Material advantage | Material disadvantage | Material used in image modality |
|------------------|---|---|---|
| PAA gel | Elastic and easily formed <ul style="list-style-type: none">Used for multi-layered sample.Inexpensive.low ↓ Temperature fluctuations. | Time stability for 5 months Requires storage in sealed glass tubes | Suitable for MRI device |
| Carrageenan gel | Easily mold to different shapes. Inexpensive. | The relaxation time different. During hardness. | Suitable for MRI device |
| PAAG gel | Provides wide sites for hydrogen. | Properties affected by temperature. | Suitable for MRI device |
| Agar gel | Hydrophilic organic materials. Easily formed by temperature. | Properties affected by temperature. Restricted movement in free water. | Suitable for MRI, US, CT and scintillation camera imaging |
| Agarose gel | Independent of temperature. Used in different shape. Stable in long period | Time stability for 5 months. More complicated components than agar. Affected by bacterial infection | Suitable for MRI and CT |
| PVA (cryogel) | Low-cost price. Stable in long time. Easily handling. | | Suitable for MRI and US |
| Polyurethane gel | High elastic recover. Resistance to | Complex in molecular design. | Suitable for US |

| Material | Material advantage | Material disadvantage | Material used in image modality |
|-------------------------------------|---|---|---|
| | bacterial infection Low. Low viscosity. | | |
| Gelatine-alginate | High Stability. Store beneath water. | Complex structure. Lack of longevity. | Suitable for US and scintillation camera |
| Silicone polymer, RTV | Robust material. High Stability for long time. Easily formed. | Mismatching with biological tissues. | Suitable for CT |
| Commercial rigid plastics | High Stability in shape. High Stability for long time. | Stiffness more than normal tissue. Complex structure. Need specific device. | Suitable for CT and scintillation camera imaging. |
| Elastomeric (rubber-like) materials | Good flexibility. Good Elasticity | Complex structure. Need specific device. | Suitable for MRI and US |

Author details

Muntaser S. Ahmad^{1*}, Osama Makhamrah² and Mohammad Hjouj²

1 Faculty of Applied Medical Health, Department of Medical Imaging, Palestine Ahliya University, Bethlehem, Palestine

2 Faculty of Health Professions, Medical Imaging Department, Al-Quds University, Jerusalem, Palestine

*Address all correspondence to: wmuntaser@gmail.com

IntechOpen

© 2021 The Author(s). Licensee IntechOpen. This chapter is distributed under the terms of the Creative Commons Attribution License (<http://creativecommons.org/licenses/by/3.0>), which permits unrestricted use, distribution, and reproduction in any medium, provided the original work is properly cited. 

References

- [1] Heimbach, J. K., Kulik, L. M., Finn, R. S., Sirlin, C. B., Abecassis, M. M., Roberts, L. R., ... & Marrero, J. A. (2018). AASLD guidelines for the treatment of hepatocellular carcinoma. *Hepatology*, 67(1), 358-380.
- [2] European Association For The Study Of The Liver. EASL clinical practice guidelines: management of hepatocellular carcinoma. *Journal of hepatology*. 2018 Jul 1;69(1):182-236.
- [3] Ahmad, M. S., Suardi, N., Shukri, A., Mohammad, H., Oglat, A. A., Abunahel, B. M., ... & Makhamrah, O. (2019). Current status regarding tumour progression, surveillance, diagnosis, staging, and treatment of HCC: a literature review. *Journal of Gastroenterology and Hepatology Research*, 8(2), 2841-2852.
- [4] Rethy, A., Sæternes, J. O., Halgunset, J., Mårvik, R., Hofstad, E. F., Sánchez-Margallo, J. A., & Langø, T. (2018). Anthropomorphic liver phantom with flow for multimodal image-guided liver therapy research and training. *International journal of computer assisted radiology and surgery*, 13(1), 61-72. DOI: 10.1007/s11548-017-1669-3.
- [5] McGarry, C. K., Grattan, L. J., Ivory, A. M., Leek, F., Liney, G. P., Liu, Y., ... & Clark, C. H. (2020). Tissue mimicking materials for imaging and therapy phantoms: a review. *Physics in Medicine & Biology*. DOI: 10.1088/1361-6560/abbd17.
- [6] Li, Y., Wang, L. H., Zhang, H. T., Wang, Y. T., Liu, S., Zhou, W. L., ... & Yang, J. Y. (2018). Disulfiram combined with copper inhibits metastasis and epithelial–mesenchymal transition in hepatocellular carcinoma through the NF- κ B and TGF- β pathways. *Journal of cellular and molecular medicine*, 22(1), 439-451. DOI: 10.1111/jcmm.13334.
- [7] Schellhaas, B., Görtz, R. S., Pfeifer, L., Kielisch, C., Neurath, M. F., & Strobel, D. (2017). Diagnostic accuracy of contrast-enhanced ultrasound for the differential diagnosis of hepatocellular carcinoma: ESCULAP versus CEUS-LI-RADS. *European journal of gastroenterology & hepatology*, 29(9), 1036-1044. DOI: 10.1097/MEG.0000000000000916.
- [8] Ayuso, C., Rimola, J., Vilana, R., Burrel, M., Darnell, A., García-Criado, Á., ... & Brú, C. (2018). Diagnosis and staging of hepatocellular carcinoma (HCC): current guidelines. *European journal of radiology*, 101, 72-81. DOI: 10.1016/j.ejrad.2018.01.025.
- [9] Paisant, A., Vilgrain, V., Riou, J., Oberti, F., Sutter, O., Laurent, V., ... & Aubé, C. (2020). Comparison of extracellular and hepatobiliary MR contrast agents for the diagnosis of small HCCs. *Journal of hepatology*, 72(5), 937-945. DOI: 10.1016/j.jhep.2019.12.011.
- [10] Ippolito, D., Querques, G., Okolicsanyi, S., Franzesi, C. T., Pecorelli, A., Lombardi, S., ... & Sironi, S. (2018). Dynamic contrast enhanced perfusion CT imaging: a diagnostic biomarker tool for survival prediction of tumour response to antiangiogenetic treatment in patients with advanced HCC lesions. *European journal of radiology*, 106, 62-68. DOI: 10.1016/j.ejrad.2018.07.012.
- [11] Choi, M. H., Choi, J. I., Lee, Y. J., Park, M. Y., Rha, S. E., & Lall, C. (2017). MRI of small hepatocellular carcinoma: typical features are less frequent below a size cutoff of 1.5 cm. *American Journal of Roentgenology*, 208(3), 544-551. DOI: 10.2214/AJR.16.16414.
- [12] Schraml, C., Kaufmann, S., Rempp, H., Syha, R., Ketelsen, D., Notohamiprodjo, M., & Nikolaou, K.

- (2015). Imaging of HCC—current state of the art. *Diagnostics*, 5(4), 513-545. DOI: 10.3390/diagnostics5040513.
- [13] Dietrich, C. F., Nolsøe, C. P., Barr, R. G., Berzigotti, A., Burns, P. N., Cantisani, V., ... & Zheng, R. (2020). Aktualisierte Leitlinien und Empfehlungen für die gute klinische Praxis für CEUS der Leber. *Ultraschall Med*, 562-585. DOI: 10.1055/a-1177-0530.
- [14] Huang, J. Y., Li, J. W., Lu, Q., Luo, Y., Lin, L., Shi, Y. J., ... & Lyshchik, A. (2020). Diagnostic accuracy of CEUS LI-RADS for the characterization of liver nodules 20 mm or smaller in patients at risk for hepatocellular carcinoma. *Radiology*, 294(2), 329-339. DOI: 10.1148/radiol.2019191086.
- [15] Sabaté-Llobera, A., Mestres-Martí, J., Reynés-Llompart, G., Lladó, L., Mils, K., Serrano, T., ... & Ramos, E. (2021). 2-[18F] FDG PET/CT as a Predictor of Microvascular Invasion and a High Histological Grade in Patients with a Hepatocellular Carcinoma. *Cancers*, 13(11), 2554. DOI: 10.3390/cancers13112554.
- [16] Ahmad, M. S., Suardi, N., Shukri, A., Mohammad, H., Oglat, A. A., Alarab, A., & Makhamrah, O. (2020). Chemical characteristics, motivation and strategies in choice of materials used as liver phantom: a literature review. *Journal of medical ultrasound*, 28(1), 7. DOI: 10.4103/JMU.JMU_4_19.
- [17] I. Computerized Imaging Reference Systems, "Triple modality 3D abdominal phantom, Model 057A.," Available from: <http://www.Cirsinc.Com/Products/Modality/65/Triple-Modality-3D-Abdominal-Phantom/>, pp. 297-300, 2017.
- [18] L. Kyoto Kagaku Co., "Abdominal Intraoperative & Laparoscopic Ultrasound Phantom 'IOUSFAN,'" Available from: <http://www.kyotokaga> ku.com/products/detail03/us-3.html, vol. 66, no. 3, pp. 373-378, 2017.
- [19] QRM for quality assurance in radiology and medicine, "QRM-Liver-Phantom," Available from: http://www.qrm.de/content/products/anthropomorphic/liver_phantom.htm, vol. 88, no. 5, pp. 606-619, 2019.
- [20] Lv, S., Long, Y., Su, Z., Zheng, R., Li, K., Zhou, H., ... & Xu, E. (2019). Investigating the accuracy of ultrasound-ultrasound fusion imaging for evaluating the ablation effect via special phantom-simulated liver tumors. *Ultrasound in medicine & biology*, 45(11), 3067-3074. DOI: 10.1016/j.ultrasmedbio.2019.07.415.
- [21] Nazem, F., Ahmadian, A., Seraj, N. D., & Giti, M. (2014). Two-stage point-based registration method between ultrasound and CT imaging of the liver based on ICP and unscented Kalman filter: a phantom study. *International journal of computer assisted radiology and surgery*, 9(1), 39-48. DOI: 10.1007/s11548-013-0907-6.
- [22] Mitchell, M. D., Kundel, H. L., Axel, L., & Joseph, P. M. (1986). Agarose as a tissue equivalent phantom material for NMR imaging. *Magnetic resonance imaging*, 4(3), 263-266. DOI: 10.1016/0730-725X(86)91068-4.
- [23] Kao, Y. H., Luddington, O. S., Culleton, S. R., Francis, R. J., & Boucek, J. A. (2014). A gelatin liver phantom of suspended 90Y resin microspheres to simulate the physiologic microsphere biodistribution of a postradioembolization liver. *Journal of nuclear medicine technology*, 42(4), 265-268. DOI: 10.2967/jnmt.114.145292.
- [24] Javan, R., & Zeman, M. N. (2018). A prototype educational model for hepatobiliary interventions: unveiling the role of graphic designers in medical 3D printing. *Journal of digital imaging*,

31(1), 133-143. DOI: 10.1007/s10278-017-0012-4.

[25] Qiu, K., Haghighashtiani, G., & McAlpine, M. C. (2018). 3D printed organ models for surgical applications. *Annual Review of Analytical Chemistry*, 11, 287-306. DOI: 10.1146/annurev-anchem-061417-125935.

[26] Shevchenko, N., Schwaiger, J., Markert, M., Flatz, W., & Lueth, T. C. (2011, January). Evaluation of a resectable ultrasound liver phantom for testing of surgical navigation systems. In 2011 Annual International Conference of the IEEE Engineering in Medicine and Biology Society (pp. 916-919). IEEE. DOI: 10.1109/IEMBS.2011.6090205.

[27] Chmarra, M. K., Hansen, R., Mårvik, R., & Langø, T. (2013). Multimodal phantom of liver tissue. *PloS one*, 8(5), e64180. DOI: 10.1371/journal.pone.0064180.

[28] Zein, N. N., Hanouneh, I. A., Bishop, P. D., Samaan, M., Eghtesad, B., Quintini, C., ... & Klatte, R. (2013). Three-dimensional print of a liver for preoperative planning in living donor liver transplantation. *Liver transplantation*, 19(12), 1304-1310. DOI: 10.1002/lt.23729.

[29] Bazrafshan, B., Hübner, F., Farshid, P., Hammerstingl, R., Paul, J., Vogel, V., ... & Vogl, T. J. (2014). Temperature imaging of laser-induced thermotherapy (LITT) by MRI: Evaluation of different sequences in phantom. *Lasers in medical science*, 29(1), 173-183. DOI: 10.1007/s10103-013-1306-5.

[30] Li, K., Su, Z., Xu, E., Huang, Q., Zeng, Q., & Zheng, R. (2017). Evaluation of the ablation margin of hepatocellular carcinoma using CEUS-CT/MR image fusion in a phantom model and in patients. *BMC cancer*, 17(1), 1-10. DOI: 10.1186/s12885-017-3061-7.

[31] Shulman, M., Cho, E., Aasi, B., Cheng, J., Nithiyantham, S., Waddell, N., & Sussman, D. (2020). Quantitative analysis of fetal magnetic resonance phantoms and recommendations for an anthropomorphic motion phantom. *Magnetic Resonance Materials in Physics, Biology and Medicine*, 33(2), 257-272. DOI: 10.1007/s10334-019-00775-x.

[32] Kamphuis, M. E., Greuter, M. J., Slart, R. H., & Slump, C. H. (2020). Quantitative imaging: systematic review of perfusion/flow phantoms. *European radiology experimental*, 4(1), 1-13. DOI: 10.1186/s41747-019-0133-2.

[33] Makhamrah, O., Ahmad, M. S., & Hjouj, M. (2019, November). Evaluation of Liver Phantom for Testing of the Detectability Multimodal for Hepatocellular Carcinoma. In *Proceedings of the 2019 2nd International Conference on Digital Medicine and Image Processing* (pp. 17-21). DOI: 10.1145/3379299.3379307.

[34] Ahmad, M. S., Makhamrah, O., Suardi, N., Shukri, A., Ab Razak, N. N. A. N., Oglat, A. A., & Mohammad, H. (2021). Hepatocellular Carcinoma Liver Dynamic Phantom For Mri. *Radiation Physics and Chemistry*, 109632. DOI: 10.1016/j.radphyschem.2021.109632.

[35] EUCLID SEERAM. *Computed Tomography: Physical Principles, Clinical Applications, And Quality Control*. 4th Edition. Elsevier Health Sciences. 2016. DOI: 978-0-323-31288-2.

[36] Hattori, K., Ikemoto, Y., Takao, W., Ohno, S., Harimoto, T., Kanazawa, S., ... & Kato, H. (2013). Development of MRI phantom equivalent to human tissues for 3.0-T MRI. *Medical physics*, 40(3), 032303. DOI: 10.1118/1.4790023.

[37] Ahmad, M. S., Suardi, N., Shukri, A., Ab Razak, N. N. A. N., Oglat, A. A., & Mohammad, H. (2020). A recent

short review in non-invasive magnetic resonance imaging on assessment of HCC stages: MRI findings and pathological diagnosis. *Journal of Gastroenterology and Hepatology Research*, 9(2), 3113-3123.

[38] Madsen, E. L., Hobson, M. A., Shi, H., Varghese, T., & Frank, G. R. (2006). Stability of heterogeneous elastography phantoms made from oil dispersions in aqueous gels. *Ultrasound in medicine & biology*, 32(2), 261-270. DOI: 10.1016/j.ultrasmedbio.2005.10.009.

[39] Blechinger, J. C., Madsen, E. L., & Frank, G. R. (1988). Tissue-mimicking gelatin-agar gels for use in magnetic resonance imaging phantoms. *Medical physics*, 15(4), 629-636. DOI: 10.1118/1.596219.

[40] Hopper, T. A., Vasilić, B., Pope, J. M., Jones, C. E., Epstein, C. L., Song, H. K., & Wehrli, F. W. (2006). Experimental and computational analyses of the effects of slice distortion from a metallic sphere in an MRI phantom. *Magnetic resonance imaging*, 24(8), 1077-1085. DOI: 10.1016/j.mri.2006.04.019.

[41] Niculescu, G., Noshier, J. L., Schneider, M. B., & Foran, D. J. (2009). A deformable model for tracking tumors across consecutive imaging studies. *International journal of computer assisted radiology and surgery*, 4(4), 337-347. DOI: 10.1007/s11548-009-0298-x.

[42] Mano, I., Goshima, H., Nambu, M., & Iio, M. (1986). New polyvinyl alcohol gel material for MRI phantoms. *Magnetic resonance in medicine*, 3(6), 921-926. DOI: 10.1002/mrm.1910030612.

[43] Groch, M. W., Urbon, J. A., Erwin, W. D., & Al-Dooan, S. (1991). An MRI tissue equivalent lesion phantom using a novel polysaccharide material. *Magnetic resonance imaging*, 9(3), 417-421. DOI: 10.1016/0730-725X(91)90430-T.

[44] Mazzara, G. P., Briggs, R. W., Wu, Z., & Steinbach, B. G. (1996). Use of a modified polysaccharide gel in developing a realistic breast phantom for MRI. *Magnetic resonance imaging*, 14(6), 639-648. DOI: 10.1016/0730-725X(96)00054-9.

[45] De Luca, F., Maraviglia, B., & Mercurio, A. (1987). Biological tissue simulation and standard testing material for MRI. *Magnetic resonance in medicine*, 4(2), 189-192. DOI:10.1002/mrm.1910040213.

[46] Goldstein, D. C., Kundel, H. L., Daube-Witherspoon, M. E., Thibault, L. E., & Goldstein, E. J. (1987). A silicone gel phantom suitable for multimodality imaging. *Investigative radiology*, 22(2), 153-157. DOI: 10.1097/00004424-198702000-00013.

[47] Yoshimura, K., Kato, H., Kuroda, M., Yoshida, A., Hanamoto, K., Tanaka, A., ... & Hiraki, Y. (2003). Development of a tissue-equivalent MRI phantom using carrageenan gel. *Magnetic Resonance in Medicine: An Official Journal of the International Society for Magnetic Resonance in Medicine*, 50(5), 1011-1017. DOI: 10.1002/mrm.10619.

[48] Talari, A. C. S., Martinez, M. A. G., Movasaghi, Z., Rehman, S., & Rehman, I. U. (2017). Advances in Fourier transform infrared (FTIR) spectroscopy of biological tissues. *Applied Spectroscopy Reviews*, 52(5), 456-506. DOI: 10.1080/05704928.2016.1230863.

[49] Lohumi, S., Lee, S., Lee, H., & Cho, B. K. (2015). A review of vibrational spectroscopic techniques for the detection of food authenticity and adulteration. *Trends in Food Science & Technology*, 46(1), 85-98. DOI: 10.1016/j.tifs.2015.08.003.

[50] Kozicki, M., Jaszczak, M., Maras, P., Dudek, M., & Cłapa, M. (2017). On the development of a VIPARnd radiotherapy 3D polymer gel dosimeter.

Physics in Medicine & Biology, 62(3), 986. DOI: 10.1088/1361-6560/aa5089.

ultrasound, 26(3), 123. DOI: 10.4103/JMU.JMU_13_17.

[51] Brunner, A. J., Blackman, B. R. K., & Davies, P. (2008). A status report on delamination resistance testing of polymer–matrix composites. *Engineering Fracture Mechanics*, 75(9), 2779-2794. DOI: 10.1016/j.engfracmech.2007.03.012.

[57] Amin, N. B., Abualroos, N. J., & Zainon, R. (2020). Fabrication of anthropomorphic thyroid-neck phantom for dosimetry study in nuclear medicine. *Radiation Physics and Chemistry*, 166, 108462. DOI: 10.1016/j.radphyschem.2019.108462.

[52] Tanikella, N. G., Wittbrodt, B., & Pearce, J. M. (2017). Tensile strength of commercial polymer materials for fused filament fabrication 3D printing. *Additive Manufacturing*, 15, 40-47. DOI: 10.1016/j.addma.2017.03.005.

[53] Bitar, R., Leung, G., Perng, R., Tadros, S., Moody, A. R., Sarrazin, J., ... & Roberts, T. P. (2006). MR pulse sequences: what every radiologist wants to know but is afraid to ask. *Radiographics*, 26(2), 513-537. DOI: 10.1148/rg.262055063.

[54] Chen, B. B., Hsu, C. Y., Yu, C. W., Liang, P. C., Hsu, C., Hsu, C. H., ... & Shih, T. T. F. (2016). Dynamic contrast-enhanced MR imaging of advanced hepatocellular carcinoma: comparison with the liver parenchyma and correlation with the survival of patients receiving systemic therapy. *Radiology*, 281(2), 454-464. DOI: 10.1148/radiol.2016152659.

[55] He, Y., Qin, S., Dyer, B. A., Zhang, H., Zhao, L., Chen, T., ... & Qiu, J. (2019). Characterizing mechanical and medical imaging properties of polyvinyl chloride-based tissue-mimicking materials. *Journal of applied clinical medical physics*, 20(7), 176-183. DOI: 10.1002/acm2.12661.

[56] Oglat, A. A., Matjafri, M. Z., Suardi, N., Oqlat, M. A., Abdelrahman, M. A., Oqlat, A. A., ... & Abujazar, M. Y. (2018). Chemical items used for preparing tissue-mimicking material of wall-less flow phantom for doppler ultrasound imaging. *Journal of medical*